OPEN

Correspondence and requests for materials should be addressed to D.W.K. (dwkim@ajou. ac.kr)

Scalable One-pot Bacteria-templating Synthesis Route toward Hierarchical, Porous-Co_3O_4 Superstructures for Supercapacitor Electrodes

Hyun-Woo Shim[1], Ah-Hyeon Lim[1], Jae-Chan Kim[1], Eunjin Jang[2], Seung-Deok Seo[1], Gwang-Hee Lee[1], T. Doohun Kim[2] & Dong-Wan Kim[1]

[1]Department of Energy Systems Research, Ajou University, Suwon, 443-749, Korea, [2]Department of Molecular Science and Technology, Graduate School of Interdisciplinary Programs, Ajou University, Suwon, 443-749, Korea.

Template-driven strategy has been widely used to synthesize inorganic nano/micro materials. Here, we used a bottom-up controlled synthesis route to develop a powerful solution-based method of fabricating three-dimensional (3D), hierarchical, porous-Co_3O_4 superstructures that exhibit the morphology of flower-like microspheres (hereafter, RT-Co_3O_4). The gram-scale RT-Co_3O_4 was facilely prepared using one-pot synthesis with bacterial templating at room temperature. Large-surface-area RT-Co_3O_4 also has a noticeable pseudocapacitive performance because of its high mass loading per area ($\sim$10 mg cm^{-2}), indicating a high capacitance of 214 F g^{-1} (2.04 F cm^{-2}) at 2 A g^{-1} (19.02 mA cm^{-2}), a Coulombic efficiency averaging over 95%, and an excellent cycling stability that shows a capacitance retention of about 95% after 4,000 cycles.

Nature offers us various and excellent biotemplates[1–3] such as bamboo, pig bone, cotton fibers, crab shells, lotus pollen grains, and butterfly wings. Such biotemplates exhibit precise widths and lengths, complex exterior and interior surfaces, and uniform geometries, all of which have inspired researchers to produce multiscale hybrid inorganic materials that exhibit hierarchical morphologies. Among such biotemplates, naturally occurring biological systems such as DNA[4,5], proteins[6], and viruses[7,8] have attracted more attention because of their abundant sources and complex structural diversities. However, they are not only expensive and difficult to use but also insufficient for the large-scale production of multiscale hybrid inorganic materials. Bacteria[9,10] are other important microorganisms found in nature, and they exhibit a large variety of well-defined stunning morphologies, *e.g.*, *bacillus*, *coccus*, *vibrio*, *spirillum*, fusiform bacilli, star-shaped bacteria, square bacteria, etc. These interesting morphologies afford us natural templates to fabricate nano/micro structures under mild conditions. Above all, the sources of bacteria are inexpensive and easy to handle, and bacteria-templated mineralization is inexpensive, environmentally friendly, and efficient and can be applied to the large-scale production of functional materials.

In the present work, we used a one-step procedure bacteria-supported mineralization at room temperature to produce three-dimensional, hierarchical, porous-Co_3O_4 superstructures with flower-like microsphere morphologies. Spherical *Micrococcus lylae* (a Gram-positive bacterium) was used as a biotemplate to mediate cobalt oxides. Furthermore, we used the porous-Co_3O_4 superstructures as an electrode material for supercapacitors, which resulted in devices with high yields and mass-loadings of active materials per unit area. Even if a few applications have been reported as electrode materials for Li-ion batteries[7,11], they have been measured with a low mass-loading of active materials per unit area, thereby leading to the practical difficulties in the applications to electrode materials for Li-ion batteries. Besides, the application of bacteria-templated Co_3O_4 as supercapacitor electrodes has rarely been reported. Therefore, a high yield and the noteworthy mass-loading of active materials per unit area are important for actual application to supercapacitors, and the preparation of unique nanostructures that can offer a large BET surface area and high pore-size distribution is also important in order to achieve excellent performance of supercapacitors, because the reactions in supercapacitors occur within several nanometers of the surfaces, unlike the case in Li-ion batteries. In particular, the bacteria used as templates here could support to retain the 3D-hierarchical structures of RT-Co_3O_4 during charge/discharge process without

major collapse, offering structural stability of the porous-Co_3O_4 superstructures as an electrode material for supercapacitors with strong cycle life at even high current density. To the best of our knowledge, such an approach toward the use of Co_3O_4 as a super-capacitor electrode material has not been reported thus far.

Results

Micrococcus-directed biomineralization. Typical field-emission scanning electron microscope (FE-SEM) and transmission electron microscope (TEM) images of an original _Micrococcus_ cell revealed an average cell diameter of 800 nm to 1 μm and a smooth, amorphous surface morphology characteristics (Fig. 1a; see also Supplementary Fig. S1). It is clear that the biomineralization of nanocrystalline Co_3O_4 onto _Micrococcus_ bacteria is closely related to the surface

properties of the cell. _Micrococcus_, as with _B. subtilis_, is one of the most extensively studied Gram-positive bacteria.

It is well known that the cell wall of many Gram-positive bacteria is primarily composed of peptidoglycans (PGs), which is a polymer of _N_-acetylglucosamine and _N_-acetylmuramic acid, and two other important anionic polymer constituents (_i.e._, teichoic acid and tei-churonic acid)[12]. In most Gram-positive bacteria, a network of anionic cell-wall polymers consisting of glucopyranosyl glycerol phosphate, called teichoic acids (TAs), is present in the cell envelope. Wall teichoic acids (WTAs) are covalently bonded by a phosphate group to the _N_-acetylmuramic acid constituent of peptidoglycans, whereas lipoteichoic acids (LTAs) are anchored by a glycolipid to the cytoplasmic membrane. Teichuronic acid is another anionic polymer similar to teichoic acid, but the phosphate functional group is
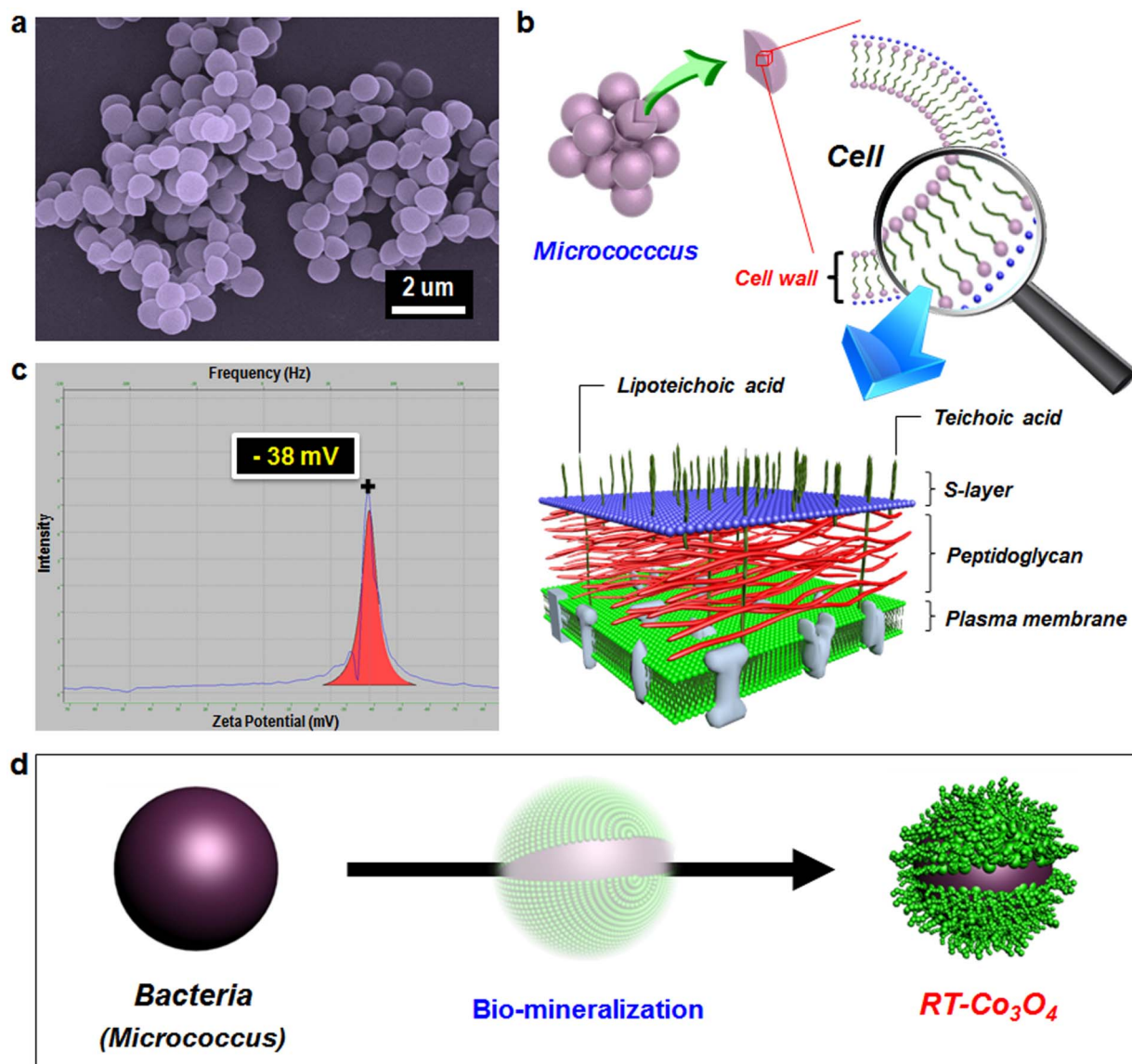

Figure 1 | Schematics of the bacteria used and the design of the 3D-hierarchical Co_3O_4 superstructure. (a), FE-SEM image of the original _Micrococcus lylae_ bacteria used as biotemplates. The diameter characteristic of _Micrococcus lylae_ is around 800 nm to 1 μm. (b), Detailed depiction of the _Micrococcus_ cell envelope. The cell wall of _Micrococcus_, as a Gram-positive bacterium, has generally well-known structures (thick peptidoglycan and S-layer) and glycopolymers (teichoic acid; TA or lipoteichoic acid; LTA). (c), Zeta-potential (ζ) for _Micrococcus_ bacteria suspended in distilled water (pH 6.5) was −38 mV, indicating the net negatively charged surface of the bacteria. (d), Schematic showing the one-pot synthesis of 3D-hierarchical Co_3O_4 structures through cobalt oxides (green) directly assembled onto bacterial surface at room temperature. The hierarchical cobalt oxides are produced by the biosorption of Co^{2+} onto the cell surfaces of _Micrococcus_ and subsequent reduction and oxidation reactions (reaction time was 12 h). FE-SEM image was taken by H.-W. Shim. The simplified illustration of the cell wall of micrococcus was drawn by J.-C. Kim. The zeta-potential was taken by H.-W. Shim. The experimental concept was drawn by J.-C. Kim.

replaced with a carboxyl group (Fig. 1b). In addition, the paracrystalline layer (S-layer) proteins present as the outermost component of the cell wall are reported to function as templates for natural mineralization and are known to bind nanoparticles[13]. Some Gram-positive bacteria such as *B. subtilis* lack a capsule and an S-layer, and thus peptidoglycan and TAs are located at the interface between the cell and its environment. Consequently, the surface of the cell walls of such bacteria is predominantly covered with carboxyl (R-COOH), phosphomonoester (R-OPO$_3$H$_2$), phosphodiester ((RO)$_2$-P(OH)$_2$), amines (R-NH$_3^+$), and hydroxyl (R-OH) functional groups[14] (Supplementary Fig. S2). These surface functional groups, associated with the polyionic networks and peptidoglycans, can contribute to the highly negative surface charge of the cell; that is, cations can be readily captured onto the bacterial surface[15,16]. Indeed, zeta-potential (ζ) measurements showed that the suspension of *Micrococcus* cells well-dispersed in distilled water displayed a highly negative value of −38 mV (Fig. 1c).

The initiating event of every biomineralization process is the formation of a precursor complex through specific interactions between a metal or metal ion and a biotemplate. As mentioned above, the anionic polymers consisting of either a phosphate or carboxyl functional group, and numerous other functional groups present in bacteria, can extensively interact with metal ions through a simple electrostatic driving force. Herein, an aqueous electroless deposition of cobalt cations (Co^{2+}) is illustrated using the metal-binding properties of the surface of *Micrococcus* cells to fabricate RT-Co$_3$O$_4$ microspheres, which retained the morphology of the original template (Fig. 1d). We believe that this hierarchical formation of Co$_3$O$_4$ nanoparticles on bacterial surfaces may be considered as "ripening and self-assembly" of cobalt oxides. Biomineralization can be determined as a possible reaction between functional groups on the bacterial surface and Co^{2+} ions by measuring the zeta-potential (Supplementary Fig. S3).

In order to characterize the possible reaction of the bacterial surface with Co^{2+} ions, UV-visible absorption spectra of the combined solutions were obtained with increasing reaction time at room temperature (Supplementary Fig. S4). A clear absorption peak around 500 nm was observed in pure CoCl$_2$·6H$_2$O solution; this peak became significantly weaker after adding the bacterial solution. In addition, the combined solution does not show any noticeable absorption after subsequent addition of the reductant NaBH$_4$ solution, which indicates the formation of Co^0 nanometals by the reduction reaction, as reported in the UV-visible spectra of cobalt nanoparticles[17,18]. Furthermore, the subsequent reduction of Co^{2+} ions by NaBH$_4$ was clearly evidenced by the systematic color change from pink to black, and the black coloration of the solution changed to dark yellow by the spontaneous air oxidation in aqueous solution with increasing reaction time[11,19] (Supplementary Fig. S5).

Characterization of Co$_3$O$_4$ microspheres. The RT-Co$_3$O$_4$ microspheres show that cobalt oxide had been uniformly deposited onto the bacterial surface in a morphology characteristic of flower-like structures, which was distinct from the smooth surface of the original bacteria (Figs. 2a, b, and inset of Fig. 2b). Most of the RT-Co$_3$O$_4$ microspheres clearly retained the form of the original spherical bacteria, except for the surface roughness of the microspheres, and did not exhibit any noticeable changes in size. However, some hollow spheres (as shown by the red arrow in Fig. 2b) also existed in the broken region because cellular fragments were probably released during the synthetic process. Moreover, the uniform deposition of Co$_3$O$_4$ nanoparticles can be easily controlled and can lead to the formation of organic/inorganic composites such as a bacteria@ Co$_3$O$_4$ core-shell system without requiring any further functionalization of the bacterial template. Interestingly, the RT-Co$_3$O$_4$ microspheres obviously exhibited hierarchical structures consisting of ∼ 2–10-nm-diameter Co$_3$O$_4$ nanoparticles, as depicted in the
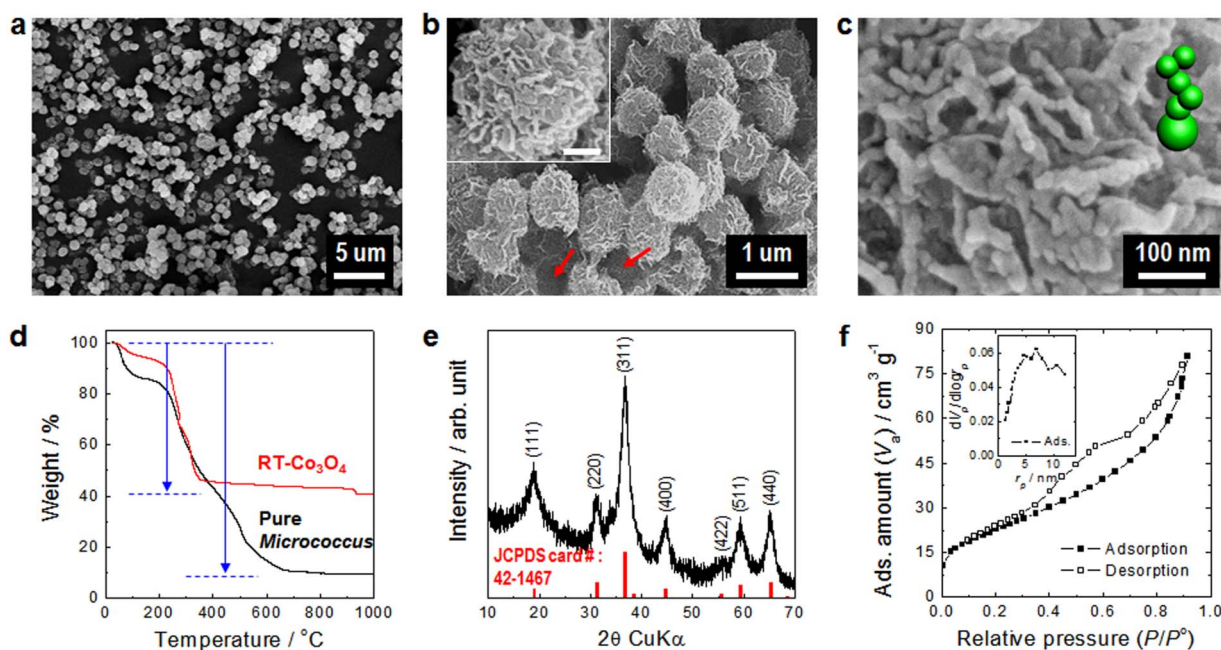

Figure 2 | Characterization of Co$_3$O$_4$ superstructure mediated by bacteria-templating. (a, b), FE-SEM images of uniform, bacteria-supported, hierarchical Co$_3$O$_4$ superstructures produced without changing the spherical shape of the original bacteria template. Low- (a) and high-magnification micrographs (b). Inset in (b) shows the morphology of an individually hierarchical, flower-like, porous-Co$_3$O$_4$ nanostructure grown on a bacterial template. The scale bar in the inset of (b) represents 200 nm. (c), An enlarged image for one of the anchored areas where the Co$_3$O$_4$ nanostructures were attached and grown on the bacterial surface. (d), TG analysis measured in air for the obtained hierarchical, porous-Co$_3$O$_4$/bacteria (RT-Co$_3$O$_4$, red line) and the original bacteria (Pure *Micrococcus*, black line). The weight loss was 59.3 and 90.6%, respectively. (e), XRD patterns for the obtained hierarchical, porous-Co$_3$O$_4$/bacteria powders. The positions of the peaks were indexed to the Co$_3$O$_4$ phase (JCPDS card #42-1467, red line). (f), The N$_2$ adsorption-desorption isotherm and the pore size distribution curve (the inset in (f)) for the obtained hierarchical, porous-Co$_3$O$_4$/bacteria powders.

schematic (Fig. 2c). It is expected that this unique architecture has a large surface area and a stable morphology because of the template-supported hierarchical structures.

The content of cobalt oxide in the RT-Co_3O_4 microspheres was estimated based on thermogravimetric analysis (TGA) of both RT-Co_3O_4 microspheres and pure *Micrococcus* cells (Fig. 2d). The total weight loss of the RT-Co_3O_4 microspheres corresponded to ~ 59.3% and was attributed to the decomposition of the bacteria; that is, the cobalt oxide comprised ~ 40.7% of the content of the microspheres by weight. However, the weight fraction of cobalt oxide in the RT-Co_3O_4 microspheres may actually be below ~ 40% because of the intrinsic inorganic components of pure bacteria, *e.g.*, P, K, S, etc. The TGA measured in air for the pure *Micrococcus* cell revealed that the amount of inorganic residues was approximately 9.4% of the weight content. The crystallographic structure of the RT-Co_3O_4 microspheres was also analyzed using powder X-ray diffraction (XRD) (Fig. 2e). The positions and relative intensities of all the diffraction peaks are consistent with the standard patterns for the pure face-centered-cubic (fcc) phase of the spinel Co_3O_4 structure whose lattice constant is a = 8.084 Å, which is good accordance with the literature values (Joint Committee for Powder Diffraction Standards (JCPDS) card no. 42–1467, space group: $Fd3m$ (227)) although it is noted that the bacteria are amorphous[16]. No diffraction peaks were associated with any other impurities, indicating the high purity of the Co_3O_4 nanoparticles produced on the RT-Co_3O_4 microspheres. In addition, the mean crystallite size was appraised to be ~ 8 nm, as calculated using the Scherrer equation and the half-width of the XRD peak corresponding to the (311) plane.

To investigate the specific porosity and textural properties of the RT-Co_3O_4 microspheres, we measured the Brunauer-Emmett-Teller (BET) N_2 adsorption-desorption isotherms for the microspheres at 77 K (Fig. 2f). The profile of the isotherms illustrates the rapid uptake of N_2 in the p/p^0 region of 0 to 0.3 followed by a representative hysteresis in the mesopore region. The results reveal that the RT-Co_3O_4 microspheres essentially contain mesopores together with a minor fraction of micropores. This finding is further supported by the Barrett-Joyner-Halenda (BJH) pore size distribution plot (for more details see Supplementary Information; Pore analysis by the BJH plot).

A typical low-magnification TEM image of the RT-Co_3O_4 microspheres was obtained to show the whole view of the 3D-hierarchical structure (Fig. 3a). The enlarged TEM images demonstrate that the fluffy coating layers; that is, Co_3O_4 nanostructures coated on the bacterial-surface template, are highly porous and include numerous nanoflakes comprised of numerous nanoparticles interconnected to form a mesoporous structure (Figs. 3b and 3c). The HR-TEM observation further revealed numerous *ca.* 2–10-nm crystalline Co_3O_4 nanoparticles and the existence of 2–8-nm interparticle mesopores in the nanoflakes (Fig. 3d). The well-resolved lattice fringes show interplanar spacings of *ca.* 2.43, 2.85, and 2.03 Å, corresponding to the (311), (220), and (400) planes of cubic Co_3O_4, respectively. This finding suggests that the RT-Co_3O_4 microspheres are highly crystalline, which is also supported by the selected-area electronic diffraction (SAED) pattern (Fig. 3e). The primary ring pattern suggests the nanoflakes and the RT-Co_3O_4 microspheres are polycrystalline.

Further insight into the microstructure of an individual RT-Co_3O_4 microsphere was also gained using a scanning transmission electron microscope (STEM) and EDS elemental mapping. The TEM image of the individual RT-Co_3O_4 microsphere obviously shows a fluffy coating layer consisting of Co_3O_4 nanostructures, which indicates a thickness of *ca.* 50 nm (Fig. 3f and inset). The thickness of such layers can be effectively controlled by varying some experimental conditions[19]. Furthermore, the high-angle annular dark-field (HAADF) STEM image and elemental mapping of Co Kα1, O Kα1, and P Kα1 clearly show that the Co_3O_4 nanostructures were uniformly distributed on the bacterial surface (Figs. 3g–j; see also Supplementary Fig. S6). It is noted that the elemental mapping of P Kα1, which relates to the anionic polymers including phosphate groups in bacterial cell wall, displays a smaller area than the other elemental mappings. However, the Co Kα1 and O Kα1 mappings show similar areas. These results suggest the biosorption of cobalt cations onto the phosphate groups and the "nucleation/self-assembly growth" of hierarchical Co_3O_4 structures.
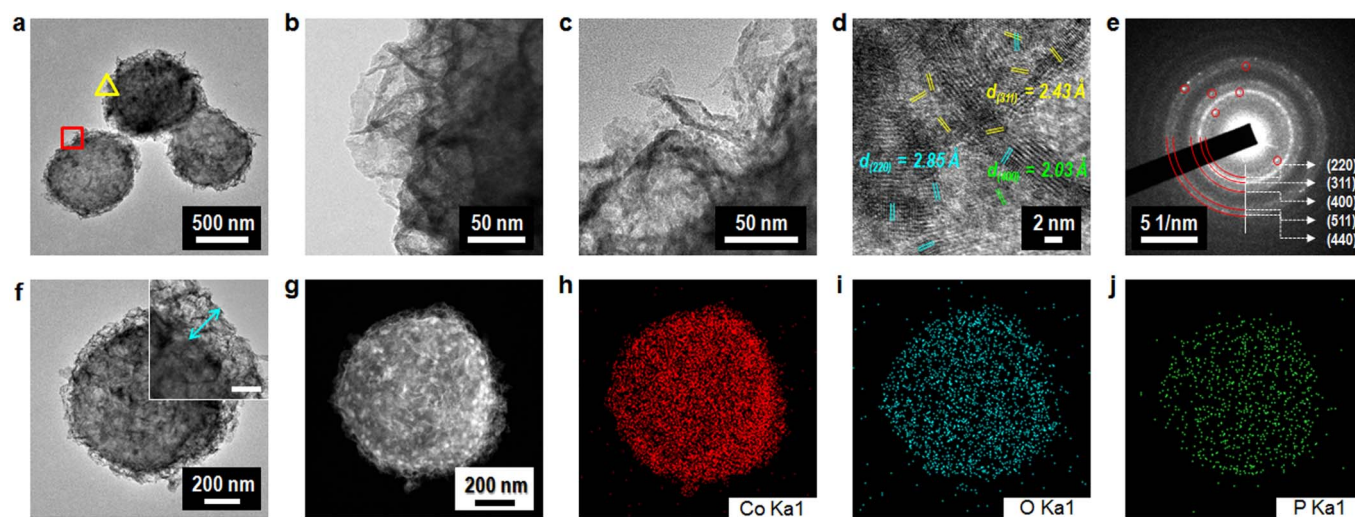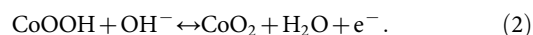

Figure 3 | TEM characterization. (a–c), TEM images of the bacteria-supported, hierarchical, porous-Co_3O_4 superstructures. Low- (a) and high-magnification micrographs (b). The images shown in (b) and (c) are open triangle (yellow line) and square (red line) regions, respectively, located in (a). The highly porous, hierarchical structures can be identified by the assembly of Co_3O_4 nanocrystals grown on the bacterial template. (d), HR-TEM image of ~ 2–10-nm nanocrystalline Co_3O_4 grains in the obtained hierarchical, porous-Co_3O_4/bacteria product. (e), The SAED pattern for the polycrystalline Co_3O_4 in the hierarchical, porous-Co_3O_4/bacteria sample. (f), An individual TEM image of the bacteria-supported, hierarchical, porous-Co_3O_4 sample. The inset shows a 3D-hierarchical Co_3O_4 layer grown on a bacterial surface (scale bar represents 50 nm). (g–j), The HAADF STEM image (g) and the EDS elemental mapping analysis (h–j) for an individual sample of the bacteria-supported, hierarchical, porous-Co_3O_4 sample shown in (f), showing the uniform distribution of Co_3O_4 nanostructures and the biosorption of cobalt ions onto a phosphate functional group associated with the negative charge of glycopolymers (see figure 1b, TA and LTA) in a bacterial cell wall.

Electrochemical performances. We then directly applied the RT-Co_3O_4 microspheres as an electrode material in supercapacitors to highlight the advantages of the unique structure of the microspheres. The electrochemical performances were evaluated using cyclic voltammograms (CVs) and galvanostatic charge-discharge measurements with high mass loading per area (~ 10 mg cm^{-2}). CVs are a suitable tool for demonstrating the capacitive behavior of any electroactive material[20]. One more pair of the broad redox peaks is shown in the CV curves for the RT-Co_3O_4–microsphere-based electrode (Fig. 4a; see also Supplementary Fig. S7), which indicates that the pseudocapacitance is mainly attributed to the reversible Faradic redox reactions of Co in different oxidation states[21,22]:

$$Co_3O_4 + OH^- + H_2O \leftrightarrow 3CoOOH + e^- \quad \text{and} \quad (1)$$

$$CoOOH + OH^- \leftrightarrow CoO_2 + H_2O + e^-. \quad (2)$$

The literature shows that two redox couples, $Co_3O_4/CoOOH$ and $CoOOH/CoO_2$, are generally involved in this system. The CV patterns, however, vary from sample to sample and strongly depend on the morphology and surface properties of the electrode[23–27]. In the present study, the peaks corresponding to each redox couple are not clearly distinguishable and some are elusive. Such broadening of some redox peaks in the CV curves may be mainly attributed to the effect of a morphology and/or microstructural properties of the electrode materials, as shown in the literature reported by Wang et al.[21], which resulted in different pseudo-capacitive performances. However, by and large, the CV characteristics of the RT-Co_3O_4-microsphere-based electrode are very consistent with those previously reported for Co_3O_4 in KOH electrolyte[21,22,28,29] and demonstrate that the overall redox reaction given by eqs. (1) and (2) are involved in the charge storage mechanism.

The specific capacitance (SC) of the electrode (see Supplementary Information; Calculation of the specific capacitance) plotted as a function of scan rate demonstrates the high-capacitive performance of the RT-Co_3O_4-microsphere-based electrode, which reveals not only the maximum specific capacitance of 1324 F g^{-1} at a scan rate of 5 mV s^{-1} but also a specific capacitance of 211 F g^{-1} at a scan rate as high as 200 mV s^{-1} (Supplementary Fig. S8). The specific capacitance of the electrode decreases with increasing scan rate because the higher scan rate prevents the ions from accessing all the pores of
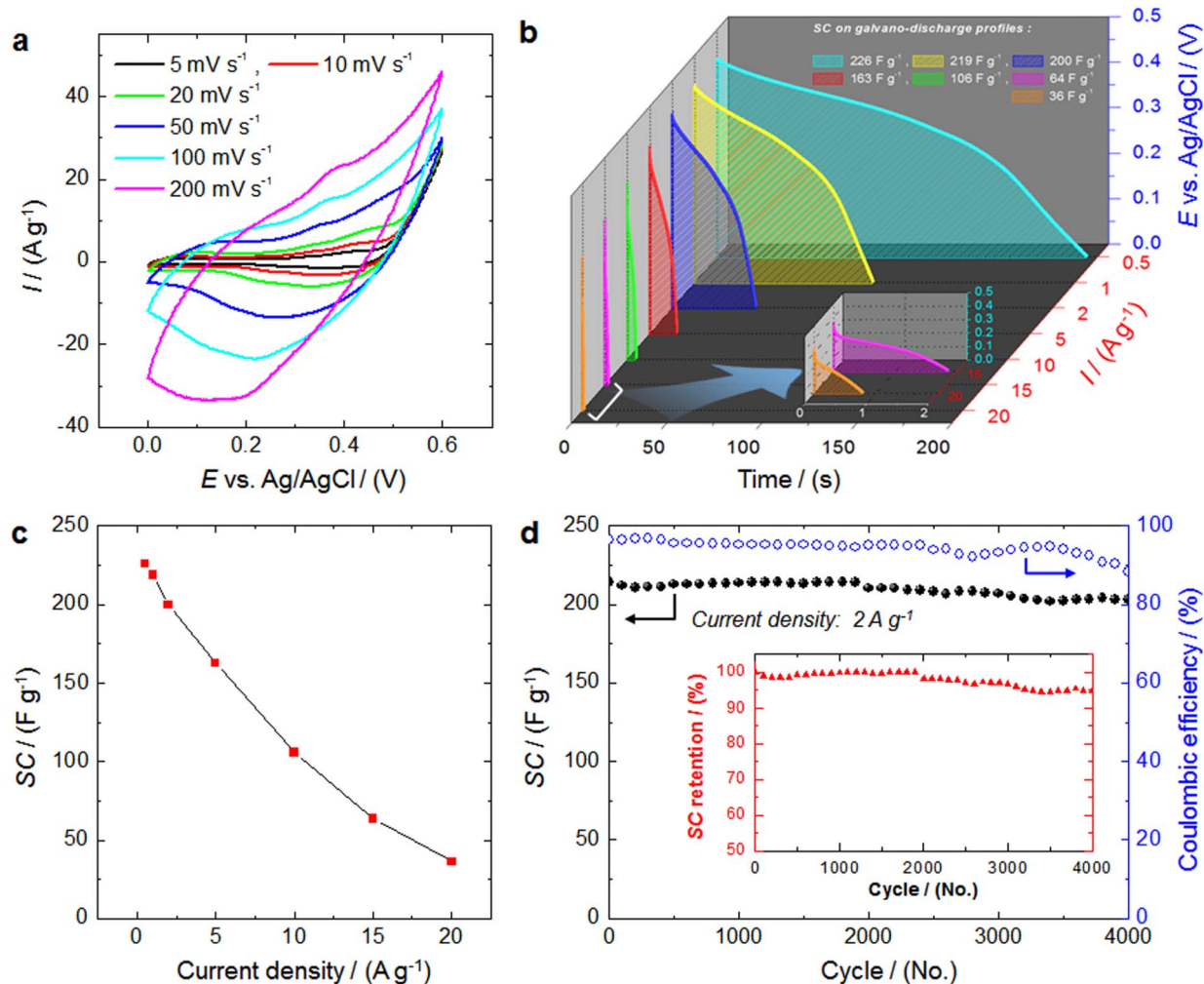

Figure 4 | Electrochemical performance. (a), Cyclic voltammograms (CVs) for the electrode produced using the bacteria-supported, hierarchical, porous-Co_3O_4 microspheres measured at six different scan rates between 5 and 200 mV s^{-1} in a 0.6-V potential window. (b), Evolution of the galvanostatic discharge profiles obtained at various current densities. The inset shows enlarged curves measured at current densities of 15 and 20 A g^{-1}. The voltage window is 0.44 V. (c), Corresponding specific capacitance (SC) *versus* current densities of the electrode produced using the bacteria-supported, hierarchical, porous-Co_3O_4 microspheres. (d), Long-term cycling performance of the 3D-hierarchical, porous-Co_3O_4/bacteria electrode (closed-circle) exhibiting a superior Coulombic efficiency (open-circle, blue line) averaging over $\sim 95\%$ at a current density of 2 A g^{-1}, and the inset shows excellent SC retention with a decrease of only $\sim 5\%$ after 4,000 consecutive cycling tests. All data were measured in a 3 M KOH aqueous solution at room temperature.

the electrode. The movement of the ions is limited because of their slow diffusion at higher scan rates, and only the outer surface can be used for charge storage.

Typical galvanostatic charge-discharge profiles were obtained at various current densities in the range 0.5–20 A g^{-1} (Fig. 4b; see also Supplementary Fig. S9). The profiles are asymmetric and triangular and exhibit broad plateaus during charging-discharging, suggesting the good pseudocapacitive behavior of the electrode. In the case of electrode materials based on transition metal oxides, it is well-known that the plateaus with sloped curves during the charge/discharge process in the working potential range indicate typical pseudo-capacitive behaviors, possibly originating from the electrochemical adsorption-desorption of electrolyte ions such as H^{+} and/or OH^{-} and/or a redox reaction on the electrode/electrolyte interface[30–32]. In detail, the sloped variation of the charge/discharge curve can be divided into plateaus and a linear variation, which correspond to the pseudo-capacitance nature resulting from the redox reaction at the electrode/electrolyte interface and double-layer capacitance behavior due to charge separation between the electrode/electrolyte interfaces, respectively. Meanwhile, in the case of electric double-layer capacitors (EDLCs), such sloped curves, involving plateaus, are not shown, that is, linear and symmetric shapes in the working potential range[33]. In this work, the slope variation of the time dependence of the working potential (from 0.0 to 0.44 V) exhibits typically sloped curves with short plateaus, indicating the good pseudo-capacitive behavior caused by the surface redox reaction of RT-Co$_3$O$_4$, which corresponds to the broad peaks of the redox pairs observed in the CV profiles.

The SC obtained at different current densities for the RT-Co$_3$O$_4$-microsphere-based electrode can be calculated based on the charge-discharge curves by equation (see Supplementary Information; Calculation of the specific capacitance) and SC is plotted as a function of current density in Fig. 4c. The RT-Co$_3$O$_4$-microsphere-based electrode exhibits quite good SCs of 226 (2.15), 219 (2.08), 214 (2.04), 163 (1.55), 106 (1.09), 64 (0.69), and 36 F g^{-1} (0.34 F cm^{-2}) at current densities of 0.5 (4.755), 1 (9.51), 2 (19.02), 5 (47.55), 10 (95.1), 15 (142.65), and 20 A g^{-1} (190.2 mA cm^{-2}), respectively. The decrease in the capacitance with increasing discharge current density is likely caused by the increase in the potential drop due to the resistance of the RT-Co$_3$O$_4$ microspheres and by the insufficient Faradic redox reaction of the active materials at higher discharge current densities. That is, ions can penetrate into the inner structure of the electrode material and gain access to almost all available pores of the electrode at lower current densities, but the effective use of the material is limited to only the outer surface of the electrode at higher current densities.

Discussion

The performance of electrochemical capacitors (ECs) is mainly determined by the electrochemical activity and kinetics of the electrodes. Therefore, to improve the energy density of ECs at high rates, it is critical to enhance the kinetics of ion and electron transport in the electrodes and at the electrode/electrolyte interface, and to engage sufficient electroactive species exposed on the surface for the Faradaic redox reaction. The RT-Co$_3$O$_4$ superstructures presented here are composed of phase-pure porous-Co$_3$O$_4$ with a flower-like morphology and hierarchical formation, which exhibited not only a remarkably large BET surface area (~149 m^2 g^{-1}) but also meso-/macroporous properties caused by the open space between the neighboring individual RT-Co$_3$O$_4$ superstructures combined with the mesoporosity present in the nanoflakes composed of small nanoparticles. This large BET surface area with high porosity can provide a large number of active sites and a large contact area for the redox reactions of Co$_3$O$_4$, which may ensure sufficient electrochemical utilizations of the RT-Co$_3$O$_4$ electrode. On the other hand, the flower-like hierarchical structure and the open meso-/macropore

space between neighboring RT-Co$_3$O$_4$ superstructures can also serve as an "ion-buffering reservoir" of OH^{-}, which ensure that sufficient Faradaic reaction can take place even at high current densities. These characteristics reduce the internal resistance, and enhance the power characteristics by shortening the diffusion path for both electrons and ions. In other words, these hierarchical porous channels can facilitate the fast penetration of the electrolytes, that is, the fast ion diffusion into the whole electrode matrix, thus enhancing the electrochemical kinetics, and also accommodate the strain arising due to high rate insertion and extraction of OH^{-} ions, and thereby leading to a strong cycling life with a high specific capacitance even at high scan rates and/or high current densities. Although a little specific capacitance deterioration that can be related to kinetic limitation on ion diffusion at high scan rates and current densities was observed during the cycling process, a high specific capacitance was fairly maintained after long-term cycling at high current densities and such superior cycling stability can be in part explained by the structural stability of the electrode, associated with Ni foam-supported the hierarchical porous-RT-Co$_3$O$_4$ superstructure electrode.

Furthermore, although the bacteria used in this study are electrochemically inactive and non-conductive, they play an important role in sustaining the structural stability for the long-term charge/discharge cycling of the electrodes, resulting in a strong cycling life, even at high constant current densities. It is generally accepted that a redox reaction that occurs during electrochemical characterization is confined to within several nanometers of the metal oxide surface[34]. In order to estimate the electrochemical utilization of the active material in this study (RT-Co$_3$O$_4$ electrode), we calculated the fraction of cobalt sites, z, which can be gauged by Faraday's law using the following relationship[35,36]:

$$z = \frac{C_S M \Delta V}{F}. \tag{3}$$

where C_s is the specific capacitance value, M is the molecular weight, ΔV is the applied potential window and F is the Faraday's constant. The value of z is 1 if all the electroactive material is involved in the redox process, that is, if all the cobalt sites have been reversibly oxidized/reduced. Using above the equation depending on the mechanism of charge storage (i.e., Co$_3$O$_4$ + OH^{-} + H$_2$O $\leftrightarrow$ 3CoOOH + e^{-}), the molecular weight of Co$_3$O$_4$ (80.26 g mol^{-1}), the specific capacitance at a current density of 2 A g^{-1} (Fig. 4d, 214 F g^{-1}) and a potential window of 0.44 V gives a z value of 0.078. In other word, 7.8% of the total active material (cobalt atoms) participates in the redox reaction for the charge storage. This low value of z suggests that the redox reaction for the charge storage in RT-Co$_3$O$_4$ occurs only at the surface of the Co$_3$O$_4$, with little bulk interaction as a result of diffusion of OH^{-} ions into the material. These results are consistent with those of studies on other metal oxides and cobalt oxide[35–37], which concluded that the redox sites of the materials are located predominately on the surface. Furthermore, calculation of the pure electric double-layer capacitance (EDLC) using an average BET specific surface area of 20 uF cm^{-2} gives an EDLC of ca. 23 F g^{-1} for hierarchical meosporous Co$_3$O$_4$ superstructures[38,39], which is significantly lower than the corresponding measured specific capacitance (214 F g^{-1} at 2 A g^{-1}) in our study. Thus, significant majority of the measured specific capacitance values originates from the Faradaic pseudo-capacitive surface redox process with RT-Co$_3$O$_4$, the pseudo-capacitance of which is up to ca. 190 F g^{-1} (i.e., 165 uF cm^{-2}).

From a comparison with the RT-300C electrodes, which were prepared via the bacterial removal process for RT-Co$_3$O$_4$ carried out at 300°C for 24 h in air, we can also confirm the bacterial effect on the pseudo-capacitive performance (Supplementary Fig. S10). This result can be caused by increased growth of Co$_3$O$_4$ nanoparticles as a result of the heat-treatment process. This increased growth resulted in the lower porosity and BET surface area of the RT-300C samples compared with the RT-Co$_3$O$_4$ samples. Indeed, we

confirmed the larger particle size of Co_3O_4 nanoparticles in RT-300C from HR-TEM images and the lower porosity and BET surface area, ~ 41 m^2 g^{-1} (Supplementary Fig. S11). Therefore, we believe that even if the bacteria were removed from the RT-Co_3O_4 *via* heat-treatment, the bacteria would not affect the capacitive performance, which might be clear evidence of the fact that the predominant redox reactions during electrochemical characterization occur only on the surface of RT-Co_3O_4.

It is also important to consider the effect of mass loading of the active material per unit area on the volumetric capacitance of the electrode in the practical application of the electrode to high-performance supercapacitors. There are numerous recent reports about self-supported cobalt-oxide electrodes for supercapacitors[21,26,27,40–42]. Such electrodes have demonstrated high-capacitance and rate capability, and their numerous advantages make them versatile. For example, the electrodes are binder-free, the current collectors can be directly assembled, and the electrodes exhibit enhanced electrical conductivity. However, the mass loading in the electrode is, in most cases, very low (*i.e.*, below ~ 2 mg cm^{-2}). Consequently, such electrodes are not favorable for application to volumetric capacitors, and the electrodes exhibit low SCs per area. Moreover, Xing et al. has recently reported that the electrodes show an exaggerated capacitance that can bring about substantial errors to specific capacitive value especially when a small amount of active materials with nickel foam as current collectors is used[43]. Upon the mass loading of active material and current density, our pseudocapacitive performance is very competitive compared with the ones reported in the literature (Supplementary Table S1.)[21,24,27,41,44]. Based on Ragone plot (for more details see Supplementary Information; Ragone plot), it is also impressive that the RT-Co_3O_4-microsphere-based electrode delivered a specific energy density from 21.9 to 3.49 W h kg^{-1} and a specific power density from 117.4 to 4,538 W kg^{-1} as the galvanostatic charge-discharge current density was increased from 0.5 to 20 A g^{-1} (Supplementary Fig. S12).

To evaluate cycling stability, we performed a constant-current charge-discharge test at a current density of 2 A g^{-1}; that is, the amount of current density actually applied to the electroactive Co_3O_4 was 6.51 A g^{-1} (Fig. 4d). The SC slightly decreased from 214 to 210 F g^{-1} (practical SC is in the range 697–684 F g^{-1} for electroactive Co_3O_4) during the first 2,000 cycles, indicating a high SC retention over 98%. More importantly, approximately 95% of the initial capacitance was retained after the electrode was continuously cycled over 4,000 times (Fig. 4d and inset). The Coulombic efficiency (see Supplementary Information; Coulombic efficiency) over *ca.* 95% during the 4,000 charge-discharge cycles clearly demonstrates the electrochemical suitability of the RT-Co_3O_4 microspheres whose redox reactions are high feasible. In addition, to further study the long-term stability of the electrodes during the charge/discharge cycles, we also evaluated electrochemical impedance spectroscopy (EIS) analyses before and after the charge/discharge tests for 4,000 cycles (Supplementary Fig. S13). Importantly, the solution resistance (R$_s$) and charge transfer resistance (R$_{ct}$) values revealed not only small but also almost the same until 4,000 cycles, indicating good electrical conductivity and OH$^-$ ion transfer of the RT-Co_3O_4, thereby leading to the superior cyclability. The detailed EIS analyses are described in the Supplementary Information; Electrochemical impedance spectroscopy (EIS) analysis.

More importantly, most of the RT-Co_3O_4 maintained its original structure and morphology without significant transformation, although minor shrinkage and collapse that can be induced by the redox reactions were observed. Furthermore, the RT-Co_3O_4 obviously revealed superior pore-distribution after the long-term cycling test on the charge/discharge process (Supplementary Fig. S14). Therefore, these results, that is, the high structural stability of the porous-Co_3O_4 superstructures, can guarantee excellent long-term cycling stability of the RT-Co_3O_4 electrodes for the charge/discharge process, even at high constant current densities (2 A g^{-1}). Furthermore, there were no noticeable changes in either the electrolyte or the electrode despite the long cycling test consisting of over 4,000 cycles (Supplementary Fig. S15). Therefore, the superior cycling stability can be in part explained by the structural stability of the microspheres, which indicates that the RT-Co_3O_4 microspheres are a promising candidate for designing high-performance supercapacitors.

In summary, we used bacteria-templating under mild conditions to develop three-dimensional, hierarchical, porous-Co_3O_4 microspheres showing flower-like structures. The ~ 2–10-nm-diameter Co_3O_4 nanoparticles were uniformly crystallized through a direct interaction between cobalt ions and bacterial surfaces, which further constructed self-assembled nanoflakes. The hierarchically structured Co_3O_4 microspheres manifest a specific surface area of *ca.* 149 m^2 g^{-1} and major mesoporous properties. These results demonstrate that the bacteria-supported route is facile, scalable, and cost-effective and that it is possible to achieve one-pot synthesis of functional inorganic materials that exhibit a large surface area and high porosity. Furthermore, the electrode produced using the hierarchical, porous-Co_3O_4 microspheres exhibited superior electrochemical performance with high pseudocapacitance and long-term cycling stability, making this electrode material one of the best for application in high-performance supercapacitors. It is also worth pointing out that the synthetic route used in the present study can be readily extended to fabricate other electroactive materials and composites.

Methods

Bacterial culture and template preparation. *Micrococcus lylae* (ATCC [27566]) and Luria-Bertani broth (LB broth, Sigma-Aldrich) were used to grow the bacterial culture. The bacteria cells (20 μL), which were stored at $-70°C$ in a deep-freezer, were first inoculated into the LB medium (20 mL) and then they were grown at 37°C in a shaking incubator (180 rpm) for 12 h. The seed-cultured cells were subsequently transferred into the LB medium (1,000 mL) to be subcultured for 10 h after which cell pellets were obtained by centrifuging the subcultured cells at room temperature and at 5,000 rpm for 20 min. The cell pellets were then resuspended in distilled water (1 L). The cell concentration was controlled by adding distilled water, adjusting the optical density (OD $_{600 nm}$) to ~ 1.65.

Fabrication of bacteria-supported, 3D-hierarchical, porous-Co_3O_4 superstructures. The bacteria-supported, hierarchical, porous-Co_3O_4 structures were prepared according to the method previously reported by our group[19]. Briefly, the hierarchical, porous-Co_3O_4 flower-like nanostructures can be facilely synthesized by adding the precursor solution (99% $CoCl_2 \cdot 6H_2O$, Sigma-Aldrich) and the reducing agent (99% $NaBH_4$, Sigma-Aldrich) to the as-prepared bacterial suspension (1 L) and by stirring the mixture at 900 rpm at room temperature. First, the precursor solution and reducing agent were separately prepared using distilled water. Then, 400 mL of the precursor solution (50 mM $CoCl_2 \cdot 6H_2O$) was slowly injected into the bacterial suspension, and the mixture was subsequently stirred for 30 min at room temperature. Then, 200 mL of the reducing agent (50 mM $NaBH_4$) was dropped into the mixture at 10 mL min^{-1}. The final mixture was vigorously stirred for 12 h at room temperature. The completely reacted final mixture was then centrifuged to collect a light-brown precipitate, which was rinsed several times with distilled water and once with acetone and was subsequently dried in a vacuum oven at 60°C for 6 h. The final product consisted of over 1 g of powder and was produced in a single batch. The powder was finely ground in an agate mortar and stored in a convection oven at 120°C for several days.

Characterization methods. The crystal phase and purity of the product were characterized using powder X-ray diffraction (XRD) with a D/max-2500V/PC X-ray diffractometer (Rigaku Co., Japan) and monochromatized Cu Kα incident radiation ($\lambda = 1.54056$ Å). The thermal behaviors of the specimens were analyzed using thermogravimetric analysis (TGA; model TA Instruments DTG-60H, Shimadzu Co., Japan). The samples used for TGA were heated from room temperature to 1,000°C in air at 5°C min^{-1}. The samples were observed under a field-emission scanning electron microscope (FE-SEM; JSM-6700F, 15 keV, JEOL, Ltd., Japan) to characterize their morphologies. The microstructure and chemical composition of the specimens were also investigated using a transmission electron microscope (TEM; model JEM-2100F, JEOL, Ltd., Japan) operated at an acceleration voltage 200 keV and equipped with an X-ray energy-dispersive spectroscopy device (EDS; model EDAX, AMETEK, Inc., USA) whose X-ray energy resolution was 132 eV. High-resolution transmission electron microscope (HR-TEM), selected-area electron diffraction (SAED) and high-angle annular dark-field (HAADF) scanning transmission electron microscope (STEM) images were acquired by scanning a specimen with a focused electron probe. In addition, N$_2$ adsorption and desorption isotherms recorded at 77 K on a

BELSORP-mini BET analyzer (BEL, Inc., Japan) were used to analyze the Brunauer-Emmett-Teller (BET) specific surface area and the Barret-Joyner-Halenda (BJH) pore size distribution of the samples, which had been predried under vacuum at 120°C for 3 h.

Electrochemical characterization. i. Fabrication of working electrode. A typical working electrode was prepared by thoroughly mixing the bacteria-supported, hierarchical, porous-Co_3O_4 powder as the active material (RT-Co_3O_4 powder, 70 wt%) together with a conductive additive (15 wt% Super-P™ carbon black; MMM Carbon, Belgium) in an agate mortar until a homogenous black powder was obtained. Here, the active material (RT-Co_3O_4 powder) was typically used 1–2 mg and mixed with commercially available Super-P™ carbon black that has an average primary particle size of 40 nm in diameter as well as BET properties of 62 $m^2 g^{-1}$ and besides, according to the technical data sheet, the Super-P™ carbon black has the high purity and structure (source, web site: http://www.timcal.com). Then, as-dissolved KYNAR 2801 binder (15 wt%, PVDF-HFP) in N-methyl-2-pyrrolidinone (NMP, Sigma-Aldrich) solvent was added to form a slurry with the mixture composed of active material and conductive carbon. To achieve uniform mixing of all components, the slurry was mixed using a homo-mixer (model Dispenser T 10 basic ULTRA-TURRAX®, © IKA®, Germany) and was also carried out by ultrasonication treatment to give enough dispersion in several times. After the solvent was briefly allowed to evaporate, the resulting paste was coated onto a piece of nickel gauze sheet as current collector and was maintained at 110°C in a vacuum oven for 6 h. The sheet was subsequently pressed under 10 MPa. Each working electrode contained the mass loadings of approximately 10 mg of the bacteria-supported, hierarchical, porous-Co_3O_4 powder and had a geometric surface area of about 1 cm^2 on the current collector.

ii. Electrochemical measurement. All electrochemical studies were performed in a beaker-type three-electrode system with an aqueous electrolyte solution (3 M KOH). The three-electrode system was connected to an electrochemical workstation (model Ivium-n-Stat electrochemical analyzer, Ivium Technologies B. V., The Netherlands). The freshly prepared bacteria-supported, hierarchical, porous-Co_3O_4 structures on nickel gauze, a platinum mesh, and an Ag/AgCl (saturated KCl) electrode served as the working, counter, and reference electrodes, respectively. Cyclic voltammograms (CVs) and galvanostatic charge-discharge cycle tests (CPs) were used to characterize the electrochemical behavior of the supercapacitor electrode. The CVs were measured between 0 and 0.6 V (vs. Ag/AgCl) at scan rates of 5, 10, 20, 50, 100, and 200 $mV s^{-1}$, and the galvanostatic charge-discharge tests were conducted in the range 0–0.44 V (vs. Ag/AgCl) with current densities of 0.5, 1, 2, 5, 10, 15, and 20 A g^{-1}. The cyclic stabilities were investigated using galvanostatic charge-discharge measurements at constant current densities of 1 and 2 A g^{-1} for over 4,000 cycles. All the electrochemical measurements were performed at room temperature.

1. Fan, T. X., Chow, S. K. & Zhang, D. Biomorphic mineralization: From biology to materials. *Prog. Mater. Sci.* **54**, 542–659 (2009).
2. Sotiropoulou, S., Sierra-Sastre, Y., Mark, S. S. & Batt, C. A. Biotemplated nanostructured materials. *Chem. Mater.* **20**, 821–834 (2008).
3. Zhou, H., Fan, T. & Zhang, D. Biotemplated materials for sustainable energy and environment: current status and challenges. *ChemSusChem* **4**, 1344–1387 (2011).
4. Dong, L. *et al.* DNA-templated semiconductor nanoparticle chains and wires. *Adv. Mater.* **19**, 1748–1751 (2007).
5. Berti, L. & Burley, G. A. Nucleic acid and nucleotide-mediated synthesis of inorganic nanoparticles. *Nat. Nanotech.* **3**, 81–87 (2008).
6. Prozorow, T. *et al.* Protein-mediated synthesis of uniform superparamagnetic magnetite nanocrystals. *Adv. Funct. Mater.* **17**, 951–957 (2007).
7. Nam, K. T. *et al.* Virus-enabled synthesis and assembly of nanowires for lithium ion battery electrodes. *Science* **312**, 885–888 (2006).
8. Dang, X. *et al.* Virus-templated self-assembled single-walled carbon nanotubes for highly efficient electron collection in photovoltaic devices. *Nat. Nanotech.* **6**, 377–384 (2011).
9. Zhou, H. *et al.* Novel bacteria-templated sonochemical route for the in situ one-step synthesis of ZnS hollow nanostructures. *Chem. Mater.* **19**, 2144–2146 (2007).
10. Berry, V. *et al.* Deposition of CTAB-terminated nanorods on bacteria to form highly conducting hybrid systems. *J. Am. Chem. Soc.* **127**, 17600–17601 (2006).
11. Rosant, C. *et al.* Biosynthesis of Co_3O_4 electrode materials by peptide and phage engineering: comprehension and future. *Energy Environ. Sci.* **5**, 9936–9943 (2012).
12. Tortora, G. J., Funke, B. R. & Case, C. L. *Microbiology: An Introduction* (10th ed., Pearson-Benjamin Cummings Publishing, 2009).
13. Shenton, W., Pum, D., Sleytr, U. B. & Mann, S. Synthesis of cadmium sulphide superlattices using self-assembled bacterial S-layers. *Nature* **389**, 585–587 (1997).
14. Jiang, W. *et al.* Elucidation of functional groups on gram-positive and gram-negative bacterial surfaces using infrared spectroscopy. *Langmuir* **20**, 11433–11442 (2004).
15. Kem, T. *et al.* Dynamics characterization of fully hydrated bacterial cell walls by solid-state NMR: evidence for cooperative binding of metal ions. *J. Am. Chem. Soc.* **132**, 10911–10919 (2010).
16. Swoboda, J. G., Campbell, J., Meredith, T. C. & Walker, S. Wall teichoic acid function, biosynthesis, and inhibition. *ChemBioChem* **11**, 35–45 (2010).
17. Bala, T., Arumugam, S. K., Pasricha, R., Prasad, B. L. V. & Sastry, M. Foam-based synthesis of cobalt nanoparticles and their subsequent conversion to $Co_{core}Ag_{shell}$ nanoparticles by a simple transmetallation reaction. *J. Mater. Chem.* **14**, 1057–1061 (2004).
18. Ershov, B. G., Sukhov, N. L. & Janata, E. Formation, absorption spectrum, and chemical reactions of nanosized colloidal cobalt in aqueous solution. *J. Phys. Chem. B* **104**, 6138–6142 (2000).
19. Shim, H. W. *et al.* Highly reversible lithium storage in *Bacillus subtilis*-directed porous Co_3O_4 nanostructures. *ACS Nano* **1**, 443–449 (2011).
20. Conway, B. E. *Electrochemical Supercapacitors: Scientific Fundamentals and Technological Applications* (Kluwer Academic/Plenum Press, 1999).
21. Wang, H. *et al.* Supercapacitive properties of hydrothermally synthesized Co_3O_4 nanostructures. *J. Phys. Chem. C* **115**, 17599–17605 (2011).
22. Rakhi, R. B., Chen, W., Cha, D. & Alshareef, H. N. Substrate dependent self-organization of mesoporous cobalt oxide nanowires with remarkable pseudocapacitance. *Nano Lett.* **12**, 2559–2567 (2012).
23. Xiong, S. *et al.* Controllable synthesis of mesoporous Co_3O_4 nanostructures with tunable morphology for application in supercapacitors. *Chem. –Eur. J.* **15**, 5320–5326 (2009).
24. Wei, T. Y. *et al.* Cobalt oxide aerogels of ideal supercapacitive properties prepared with an epoxide synthetic route. *Chem. Mater.* **21**, 3228–3233 (2009).
25. Wang, G. *et al.* Highly ordered mesoporous cobalt oxide nanostructures: synthesis, characterisation, magnetic properties, and applications for electrochemical energy devices. *Chem.–Eur. J.* **16**, 11020–11027 (2010).
26. Yuan, C. *et al.* Growth of ultrathin mesoporous Co_3O_4 nanosheet arrays on Ni foam for high-performance electrochemical capacitors. *Energy Environ. Sci.* **5**, 7883–7887 (2012).
27. Xia, X. H. *et al.* Mesoporous Co_3O_4 monolayer hollow-sphere array as electrochemical pseudocapacitor material. *Chem. Commun.* **47**, 5786–5788 (2011).
28. Hou, L. *et al.* Urchin-like Co_3O_4 microspherical hierarchical superstructures constructed by one-dimension nanowires toward electrochemical capacitors. *RSC Adv.* **1**, 1521–1526 (2011).
29. Yang, Q. *et al.* Hierarchical Co_3O_4 nanosheet@nanowire arrays with enhanced pseudocapacitive performance. *RSC Adv.* **2**, 1663–1668 (2012).
30. Zhao, D. D., Bao, S. J., Zhou, W. J. & Li, H. L. Preparation of hexagonal nanoporous nickel hydroxide film and its application for electrochemical capacitor. *Electrochem. Commun.* **9**, 869–874 (2007).
31. Sugimto, W., Iwata, H., Yasunaga, Y., Murakami, Y. & Takasu, Y. Preparation of ruthenic acid nanosheets and utilization of its interlayer surface for electrochemical energy storage. *Angew. Chem. In. Ed.* **42**, 4092–4096 (2003).
32. Zhang, G. Q., Zhao, Y. Q., Tao, F. & Li, H. L. Electrochemical characteristics and impedance spectroscopy studies of nano-cobalt silicate hydroxide for supercapacitor. *J. Power Sources* **161**, 723–729 (2006).
33. Shukla, A. K., Sampath, S. & Vijayamohanan, K. Electrochemical supercapacitors: energy storage beyond batteries. *Curr. Sci.* **79**, 1656–1661 (2000).
34. Simon, P. & Gogotsi, Y. Materials for electrochemical capacitors. *Nat. Mater.* **7**, 845–854 (2008).
35. Srinivasan, V. & Weidner, J. W. Capacitance studies of cobalt oxide films formed via electrochemical precipitation. *J. Power Sources* **108**, 15–20 (2002).
36. Srinivasan, V. & Weidner, J. W. Studies on the capacitance of nickel oxide films: effect of heating temperature and electrolyte concentration. *J. Electrochem. Soc.* **147**, 880–885 (2000).
37. Lin, C., Ritter, J. A. & Popov, B. N. Characterization of sol-gel-derived cobalt oxide xerogels as electrochemical capacitors. *J. Electrochem. Soc.* **145**, 4097–4102 (1998).
38. Cao, L., Lu, M. & Li, H. L. Preparation of mesoporous nanocrystalline Co_3O_4 and its applicability of porosity to the formation of electrochemical capacitance. *J. Electrochem. Soc.* **152**, A871–A875 (2005).
39. Li, H. Q., Luo, J. Y., Zhou, X. F., Yu, C. Z. & Xia, Y. Y. An ordered mesoporous carbon with short pore length and its electrochemical performances in supercapacitor applications. *J. Electrochem. Soc.* **154**, A731–A736 (2007).
40. Lu, Z. *et al.* Hierarchical Co3O4@Ni-Co-O supercapacitor electrodes with ultrahigh specific capacitance per area. *Nano Res.* **5**, 369–378 (2012).
41. Wei, T. Y. *et al.* A cost-effective supercapacitor material of ultrahigh specific capacitances: spinel nickel cobaltite aerogels from an epoxide-driven sol–gel process. *Adv. Mater.* **22**, 347–351 (2010).
42. Xia, X. *et al.* Freestanding Co_3O_4 nanowire array for high performance supercapacitors. *RSC Adv.* **2**, 1835–1841 (2012).
43. Xing, W. *et al.* Exaggerated capacitance using electrochemically active nickel foam as current collector in electrochemical measurement. *J. Power Sources* **196**, 4123–4127 (2011).
44. Meher, S. K. & Rao, G. R. Ultralayered Co_3O_4 for high-performance supercapacitor applications. *J. Phys. Chem. C* **115**, 15646–15654 (2011).

Acknowledgments

Author contributions

H.-W.S. performed, analyzed the experiments and drafted the manuscript. A.-H.L. prepared oxide samples and performed TGA and BET experiments. J.-C.K. carried out drawing illustrations for experimental concepts. S.-D.S. and G.-H.L. participated in microstructural and electrochemical analyses. E.J. and T.D.K. developed and optimized the bacterial culture and template preparation. D.-W.K. conceived and designed the study, led the discussion of the results, and performed the final edits of the manuscript. All authors made critical contributions to the work, discussed the results and commented on the manuscript.

Additional information

Supplementary information accompanies this paper at http://www.nature.com/scientificreports

Competing financial interests: The authors declare no competing financial interests.

How to cite this article: Shim, H. *et al.* Scalable One-pot Bacteria-templating Synthesis Route toward Hierarchical, Porous-Co$_3$O$_4$ Superstructures for Supercapacitor Electrodes. *Sci. Rep.* **3**, 2325; DOI:10.1038/srep02325 (2013).